Aggregation and Sedimentation of Aqueous Nanoscale Zerovalent Iron Dispersions

TANAPON PHENRAT,[†] NAVID SALEH,[†]
KEVIN SIRK,[‡] ROBERT D. TILTON,[‡,§] AND
GREGORY V. LOWRY*,[†]

*Departments of Biomedical Engineering, Chemical
Engineering, and Civil and Environmental Engineering,
Carnegie Institute of Technology, Carnegie Mellon University,
Pittsburgh, Pennsylvania 15213-3890*

Nanoscale zerovalent iron (NZVI) rapidly transforms many environmental contaminants to benign products and is a promising in-situ remediation agent. To be effective, NZVI should form stable dispersions in water such that it can be delivered in water-saturated porous media to the contaminated area. Limited mobility of NZVI has been reported, however, attributed to its rapid aggregation. This study uses dynamic light scattering to investigate the rapid aggregation of NZVI from single nanoparticles to micrometer size aggregates, and optical microscopy and sedimentation measurements to estimate the size of interconnected fractal aggregates formed. The rate of aggregation increased with increasing particle concentration and increasing saturation magnetization (i.e., the maximum intrinsic magnet moment) of the particles. During diffusion limited aggregation the primary particles (average radius = 20 nm) aggregate to micrometer-size aggregates in only 10 min, with average hydrodynamic radii ranging from 125 nm to 1.2 μm at a particle concentration of 2 mg/L (volume fraction(Φ) = 3.2×10^{-7}) and 60 mg/L ($\Phi = 9.5 \times 10^{-6}$), respectively. Subsequently, these aggregates assemble themselves into fractal, chain-like clusters. At an initial concentration of just 60 mg/L, cluster sizes reach 20–70 μm in 30 min and rapidly sedimented from solution. Parallel experiments conducted with magnetite and hematite, coupled with extended DLVO theory and multiple regression analysis confirm that magnetic attractive forces between particles increase the rate of NZVI aggregation as compared to nonmagnetic particles.

Introduction

The ability of nanoscale zerovalent iron (NZVI) particles to rapidly dechlorinate chlorinated organics or to immobilize heavy metals found in contaminated groundwater is well documented (*1–3*) and initial field demonstrations are promising (*4*). The high surface area and resulting high reactivity of NZVI makes it a promising and flexible technology for in-situ remediation of groundwater contaminants that are amenable to reduction by Fe⁰. High reactivity alone, however, is not sufficient to make NZVI a good in-situ

remediation agent. NZVI must also be readily dispersible in water such that it can migrate through water-saturated porous media to the contaminated area. Recent studies have reported limited mobility of NZVI particles in saturated porous media, i.e., practical transport distances of only a few centimeters or less for bare unsupported particles (*5*). There are two likely explanations for the poor transport of NZVI in water-saturated porous media. First, NZVI can be filtered from solution by attachment to aquifer materials (*6*). Second, aggregation and subsequent gelation (formation of a particle network) could cause pore plugging which limits transport (*7*).

Colloidal stability is operationally defined as the ability of a particle dispersion to resist aggregation for a specified time (*8*). Colloidal stability is promoted by the existence of an energy barrier in the interparticle interaction potential. According to conventional DLVO theory, the net interaction energy between particles is the sum of van der Waals attraction and electrostatic double layer repulsion and depends on the size, Hamaker constant, and surface potential of the particles, and on the solution ionic strength. NZVI exposed to water acquires an oxide shell, resulting in Fe⁰/Fe-oxide core/shell particles. Reactive nanoscale iron particles (RNIP) manufactured by Toda Kyogo, Japan, have a Fe⁰ core and a magnetite (Fe_3O_4) shell (*1*, *9*). Both Fe⁰ and Fe_3O_4 are magnetic (*10–12*) so magnetic attractive forces between particles may also affect the dispersion stability (*13*). The influence of the magnetic properties of iron nanoparticles on their aggregation is apparent under an applied magnetic field, where ferromagnetic or paramagnetic dispersions form chain-like aggregates in which the dipoles are oriented in a head–tail configuration along the direction of the field (*13–15*). Even in the absence of a magnetic field, chain-like aggregation of magnetic nanoparticles is commonly observed (*1*, *9*, *16*) albeit after drying. This behavior is consistent with theoretical calculations (*15*) and molecular dynamics simulations (*17*) that predict this phenomenon. Thus, in addition to conventional DLVO forces acting on the particles, an NZVI dispersion might undergo dipole–dipole attraction between the magnetic moments of the particles which may affect their size and dispersion stability.

Under certain conditions, aggregation can result in the assembly of a large network of fractal aggregates. This process is called gelation (*8*, *18*, *19*). Gelation of the chain-like aggregates to form a fractal network can enhance gravitational sedimentation (*19*). Gelation can also affect the rheological properties of the dispersion such as viscosity (*20*), which could also limit their mobility. Once injected into a porous medium, the cross-linked structure of a gelled NZVI dispersion could create an impermeable barrier and thus plug the pore spaces in an aquifer, further limiting mobility (*21*). Understanding aggregation and gelation dynamics, as well as the size and morphology of the resulting aggregates, is crucial to predicting their mobility in water-saturated porous media.

The aggregation, gelation, and sedimentation of NZVI dispersions used for in-situ groundwater remediation have not been reported. The objectives of this study are to (1) determine the aggregation rate and observe the aggregates formed during diffusion-limited aggregation (DLA) of NZVI to micrometer-sized clusters and the subsequent gelation of these clusters into chain like aggregates (under DLA, no energy barriers to attachment exist and when two particles collide they aggregate), (2) to determine the effect of NZVI dispersion concentration on the rate of aggregation and the size of the aggregates formed, and (3) to evaluate the importance of magnetic attractive forces on the rate of NZVI

* Corresponding author phone: 412-268-2948; fax 412-268-7813; e-mail: glowry@cmu.edu.
† Civil & Environmental Engineering.
‡ Chemical Engineering.
§ Biomedical Engineering.

aggregation. Dynamic light scattering (DLS) is used to monitor aggregate evolution from nanosized primary particles to micrometer-sized aggregates. Optical microscopy and NZVI sedimentation rates observed by UV−vis spectrophotometry are used to estimate the size of the NZVI aggregates formed. NZVI dispersion concentrations ranged from 2 to 1320 mg/L. The high end of this range (g/L) represents that which would be used in NZVI field application for in-situ groundwater treatment. The influence of the magnetic attractive forces between NZVI particles on aggregate formation is assessed by comparing the aggregation of NZVI with less magnetic (magnetite) and nonmagnetic (hematite) iron nanoparticles with similar colloidal properties aside from their magnetization. Factor analysis and extended DLVO theory that includes the effect of magnetic dipole−dipole interactions are used to explain the rapid aggregation and gelation observed in NZVI dispersions.

Materials and Methods

Iron-Based Nanoparticles and Dispersions. RNIP, a commercially available reactive Fe^0/Fe_3O_4 core−shell NZVI particle, was provided by Toda Kyogo, Japan. The physical and chemical properties of RNIP have been previously reported (1, 9). Magnetite (Fe_3O_4) and hematite ($\alpha\text{-}Fe_2O_3$) nanoparticles were obtained from Nanostructured and Amorphous Materials Inc (Los Alamos, NM). Aqueous dispersions (2−1320 mg/L) of RNIP, magnetite, and hematite nanoparticles were prepared in a 1 mM $NaHCO_3$ solution (pH 7.4) without deaeration. Prior to use, RNIP had been stored as an aqueous slurry at 6 g/L for 5 months in a sealed container. From this slurry, a stock dispersion (3 g/L) was prepared in 1 mM $NaHCO_3$ followed by ultrasonication for 30 min to break aggregates formed during storage. The stock dispersion was then pre-settled for 5 min to remove the largest particles ($>\sim2\ \mu m$). Magnetite and hematite were available as powder, so a stock dispersion (3 g/L) was prepared by adding a weighed mass of powder to a 1 mM $NaHCO_3$ solution. The total iron ($Fe^0 + Fe$-oxides) concentration in each of these stock solutions was determined by atomic absorption spectrometry after acid digestion in concentrated HCl (trace metal grade). Dispersions for analysis were prepared by diluting the stock dispersions in 1 mM $NaHCO_3$ to the desired concentration. Each dispersion was sonicated for 1 min just prior to DLS, optical microscopy, or the sedimentation experiments.

Particle Characterization. The magnetic properties, electrophoretic mobility, particle size, hydrodynamic radius, and Fe^0 content were determined at 25 °C (298 K). The saturation magnetization and coercivity were analyzed by superconducting quantum interference device (SQUID) (22). With SQUID, magnetization is determined as a function of applied magnetic field between ±3980 kA/m. The saturation magnetization is the maximum induced magnetic moment for a material when all magnetic domains in a particle are aligned parallel. A magnetic field of the opposite direction is then applied to reduce the remanent magnetization to zero. This demagnetizing field is the coercivity. The electrophoretic mobility was measured for dilute dispersions (~30 mg/L) in 1 mM $NaHCO_3$ with a Malvern Zetasizer (Southborough, MA). Measured electrophoretic mobilities were converted to apparent ζ-potentials using the Helmholtz−Smoluchowski relationship.

DLS (Malvern Zetasizer, Southborough, MA) was used to monitor the time-dependent hydrodynamic diameter of aggregates during the early stage of aggregation where the nanoparticles are too small to be investigated by the optical microscope. Dilute samples (2−75 mg/L) were used in order to avoid multiple scattering which can make data interpretation difficult. The CONTIN algorithm was used to convert intensity autocorrelation functions to intensity-weighted

TABLE 1. Physical Properties of Iron-Based Nanoparticles and Dispersions in 1 mM $NaHCO_3$ at pH 7.4.

sample	composition	average diameter (nm)	average density (g/cm³)	zeta potential (mV)	saturation magnetization (kA/m)
RNIP	14.3/85.7% (Fe^0/Fe_3O_4)	40[a]	6.15[b]	−31.7 ± 0.8[d]	570
magnetite	98+% (Fe_3O_4)	27.5[c]	4.95[c]	−38.2 ± 1.1	330
hematite	98+% ($\alpha\text{-}Fe_2O_3$)	40[c]	5.24[c]	−39.0 ± 0.6	14

[a] Nurmi et al., ref 9. [b] Reported by Toda Kyogo (Japan). [c] Reported by Nanostructured and Amorphous Materials Inc (USA). [d] Errors bars represent one standard deviation based on three measurements.

particle hydrodynamic diameter distributions, assuming the Stokes−Einstein relationship for spherical particles.

The Fe^0 content of RNIP was determined (separately from total iron) by acid digestion in a closed container with headspace. H_2 produced from the oxidation of Fe^0 in RNIP by H^+ is used to quantify the Fe^0 content of the particles (1).

In-Situ Optical Microscopy. The aggregation and gelation of RNIP dispersions were observed in-situ using optical microscopy (Nikon Eclipse TE300, Hauppauge, NY). A 4.5-mL capped UV−vis cuvette containing 4-mL of a RNIP dispersion at concentrations ranging from 60 to 425 mg/L was placed horizontally into the microscope. Images of RNIP aggregates in the dispersion were recorded 15/sec for 35 min at 400× magnification. All measurements were conducted at 25 °C.

Sedimentation. Nanoparticle (RNIP, magnetite, or hematite) sedimentation was determined for concentrations ranging from 2 mg/L ($\Phi = 3.2 \times 10^{-7}$) to 1320 mg/L ($\Phi = 2.1 \times 10^{-4}$) by monitoring the optical absorbance at 508 nm as a function of time by UV−vis spectrophotometery (Varian, Palo Alto, CA). All measurements were made at 25 °C. Standard curves (absorbance vs concentration) for RNIP, magnetite, and hematite are provided in the Supporting Information (Figure S1).

Multiple Regression Analysis. To determine the significant parameters governing the different aggregation rates for RNIP, magnetite, and hematite, multiple regression analysis was performed using the Statistical Package for Social Sciences (SPSS for Windows, Version 12; SPSS Inc., Chicago). The dependent parameter (dispersion stability) was regressed against the independent physical properties of the nanoparticles which should influence the colloid aggregation and sedimentation rates, including volume fraction (Φ), ζ-potential, particle diameter (r), particle density (ρ_s), and saturation magnetization (M_s). The data were linearized using a common logarithm prior to regression analysis. Unstandardized regression coefficients (B) and standardized regression coefficient (β') are reported with two-tailed p-values (p). A p-value less than 0.05 is considered statistically significant.

Results and Discussion

Particle Properties. The physical properties of each iron nanoparticle are summarized in Table 1. Given the age of the particles, the measured Fe^0 content (14%) is less than the manufacturer reported value of 60%. This is due to the oxidation of Fe^0 by water to more oxidized iron oxide phases such as Fe_3O_4 (dominant), $\gamma\text{-}Fe_2O_3$, and $\gamma\text{-}FeOOH$ (1, 9, 23) during storage in water. The saturation magnetization (M_s) of RNIP (570 kA/m) lies between that of magnetite (330 kA/m) and Fe^0 (1226 kA/m (12)), consistent with its Fe^0/Fe_3O_4 core−shell structure and the low Fe^0 content (14%) of the
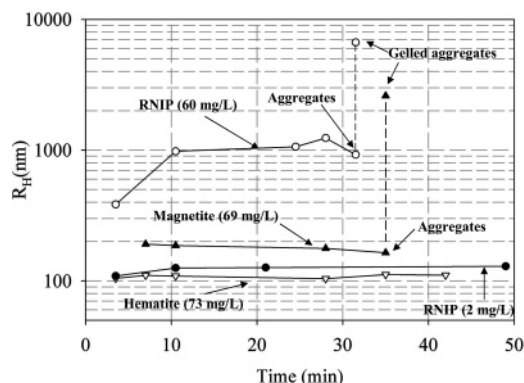
FIGURE 1. Evolution of the average R_H of dominant size class as a function of time for RNIP, magnetite, and hematite at pH 7.4. The particle size distribution for RNIP and magnetite becomes bimodal at the last measured point due to gelation of aggregates.

aged particles. Particles that had been stored in an anaerobic chamber at pH 11 for ~3 months had a higher Fe^0 content (23%) and a M_s of 720 kA/m (Supporting Information Figure S2). The M_s of hematite is ~0 as it is not ferromagnetic.

The size of the magnetite and hematite nanoparticles used here are below the critical size needed for multiple magnetic domains, which are 80 nm and 15 μm, respectively (24, 25) Thus, they are assumed to be single magnetic domain particles. For particles with multiple magnetic domains, the magnetic moment of these domains can be aligned randomly and cancel each other out, resulting in a decrease in, or absence of, the apparent magnetization (10). Single domain particles can have only one magnetic domain so the observed magnetization is equal to the intrinsic saturation magnetization (10) which can be used to estimate the magnitude of the magnetic attractive force between the particles. RNIP is a complex mixed phase (Fe^0/Fe_3O_4) particle, and distinguishing between single domain and multiple domain particles is not simple, but can be evaluated from the remanent magnetization (M_r), saturation magnetization (M_s), and coercivity (H_c), obtained from the hysteresis cycle of the magnetization loop using SQUID (Supporting Information Figure S2). The ratio of M_r/M_s for RNIP is 0.13 while its H_c is 12.6 mT. Based on these magnetic parameters, RNIP is pseudo-single domain ($0.1 < M_r/M_s < 0.5$, and $10 < H_c < 15$ mT), and the saturation magnetization can be used to estimate the magnitude of the magnetic attractive force between the particles (24, 25)

Regimes of NZVI Aggregation and Subsequent Chain-Like Gelation. Based on our observation, there are two phases of NZVI aggregation. First, the NZVI rapidly aggregates to form discrete, micrometer-sized aggregates. This is followed by the linking of each of these aggregates into chains, or gelation (Supporting Information Figure S3). Supporting evidence for these regimes are discussed below.

First Regime: Aggregation of NZVI Particles to Discrete Micrometer-Sized Aggregates. The particle size distribution (geometric mean hydrodynamic diameter) was monitored by DLS over time for RNIP, magnetite, and hematite dispersions ranging in concentration from 2 to 74 mg/L. The growth of the average hydrodynamic radius, R_H, (one half of the measured hydrodynamic diameter) for RNIP, magnetite, and hematite are shown in Figure 1. The evolution of intensity-averaged particle size distributions (i.e., the raw data) for each particle type is provided in the Supporting Information (Figure S4). For times less than 30 min, a monomodal distribution of particle hydrodynamic radii were observed for all three types of particles. For RNIP and magnetite at concentrations of 60 mg/L and 69 mg/L, respectively, a bimodal distribution appears after 30 min. This is when the system transitions from the first regime to the second regime (chain formation and gelation), with the

mode with smaller R_H being particle aggregates and the mode with larger R_H being gelled aggregates (Figure S4b and S4c).

At low concentration (2 mg/L, volume fraction (Φ) = 3.2 × 10^{-7}) RNIP has an initial average R_H of 109 nm. Because the range of radii for individual RNIP particles are from 5 to 40 nm (average radius = 20 nm) (9), an average R_H of 109 nm observed after only 3.5 min (Figure 1) indicates that the primary RNIP particles rapidly aggregate. Primary RNIP particles with R_H ranging from 9 to 15 nm are observed (Figure S4a), but at a very low intensity (0.2%). As aggregation proceeds, the average R_H reaches a stable size of ~125 nm after 10 min (Figure 1). The rate of aggregation and the stable size of the individual aggregates formed increases with increasing particle concentration. At an initial RNIP concentration of 60 mg/L (Φ = 9.5 × 10^{-6}) the stable average R_H was 1.2 μm compared to 125 nm for 2 mg/L (Φ = 3.2 × 10^{-7}) (Figure 1). This is consistent with theory which predicts that the aggregation rate has a second-order dependence on particle concentration (8).

The evolution of the particle size distribution for magnetite also showed a monomodal distribution in the first regime and bimodal distributions upon transition to the second regime (Figure S4c in the Supporting Information). In contrast to RNIP and magnetite, the evolution of particle size distribution of hematite showed only a monomodal distribution, and no transition to the second regime was observed after 2 h at an initial concentration of 73 mg/L (Figure S4d in the Supporting Information). The stable average R_H for magnetite and hematite at 69 mg/L (Φ = 1.4 × 10^{-5}) and 73 mg/L (Φ = 1.4 × 10^{-5}) are 185 and 110 nm, respectively, after 7 min (Figure 1). Comparing the aggregate sizes for RNIP, magnetite, and hematite at similar concentrations (~70 mg/ L), the average R_H of the aggregates increases as the saturation magnetization of the particles increases, hematite < magnetite < RNIP. Because the physical properties of the particle types are similar (size and zeta potential), magnetic attractive forces between the particles are likely responsible for the difference. The effect of magnetizm is explored further later in this study.

The individual submicrometer or micrometer-size aggregates that form in the first 20−30 min ultimately become the primary units forming the chain-like clusters in the second aggregation regime. The transition from the first regime of aggregation to the second regime of gelation, although studied in dilute dispersions, can be expected to occur in concentrated dispersions of these iron-based nanoparticles, although they should occur at a faster rate as discussed next.

Second Regime: Chain Formation and Gelation of Micrometer-Size Aggregates. The formation of larger chain-like fractal aggregates from the individual micrometer-sized aggregates formed in regime 1 was observed in a 60 mg/L (Φ = 9.5 × 10^{-6}) RNIP dispersion with a light microscope (Figure 2). At this concentration, micrometer-size clusters are observed after only 1 min followed by the aggregation of these clusters into doublets or triplets, and finally into chain-like fractal aggregates (Figure 2c and d). For DLA, the R_H of the micrometer-sized fractal aggregates formed at a particular time can be approximated using eqs 1 and 2 (26)

$$R_G = R_o\sqrt{\frac{D_f}{D_f + 2}} \qquad (1)$$

$$\frac{R_H}{R_G} = 0.875 \qquad (2)$$

where R_G is the radius of gyration, the radius of a dense sphere which has the same mass as the fractal aggregate of interest. R_o is one half of the observed fractal aggregate diameter at the time of interest. At 3.75 min (Figure 2b), R_o
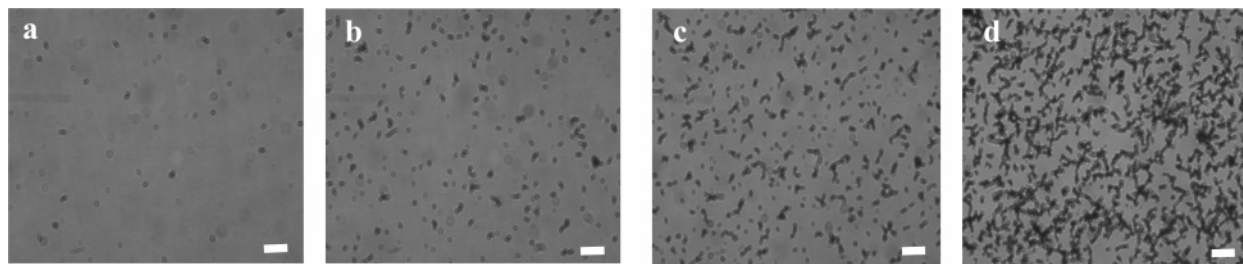
FIGURE 2. In-situ micrographs illustrating aggregation kinetics of the dispersion of RNIP at 60 mg/L (pH 7.4, $\Phi = 10^{-5.02}$): (a) time (t) = 1 min; (b) t = 3.75 min; (c) t = 9 min; and (d) t = 30 min. Scale bar = 25 μm.
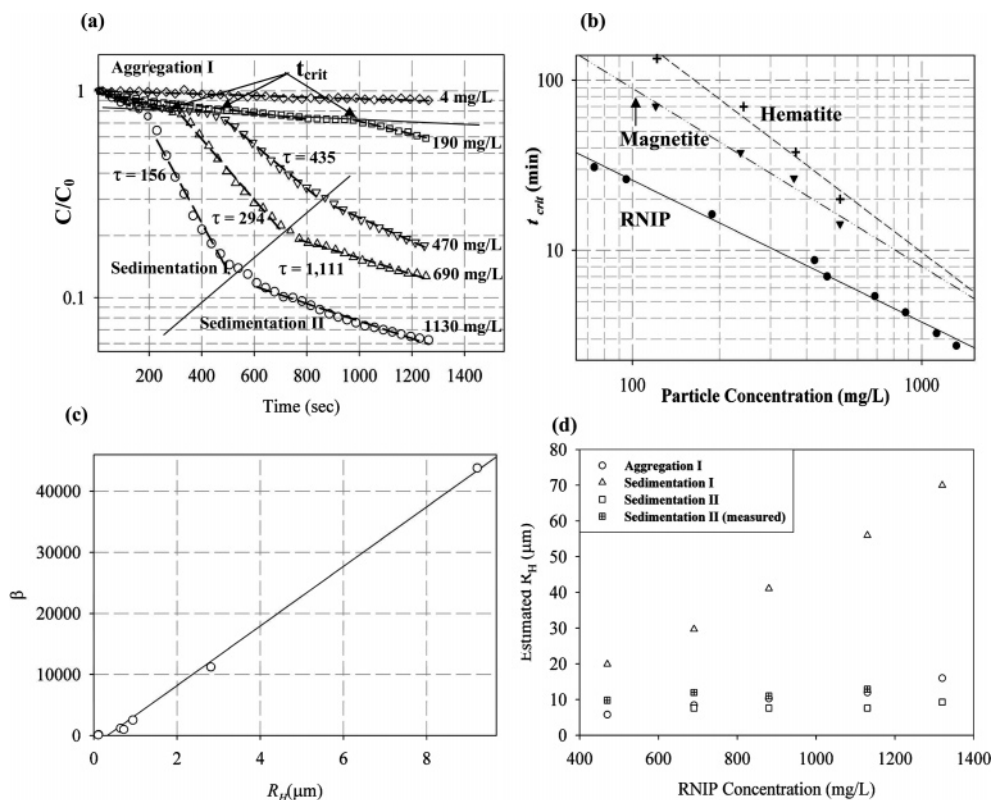

FIGURE 3. (a) Sedimentation curves of RNIP at various initial concentrations (semilog); (b) relationship between t_{crit} and particle concentration for RNIP, magnetite, and hematite (log−log); (c) empirical relationship between R_H and β determined for dilute RNIP dispersions; (d) predicted and measured R_H for concentrated RNIP dispersions in the three different sedimentation regions. Open symbols are predicted values. Hashed squares are the values determined by DLS on samples taken after 2 h during Sedimentation II.

ranged from 2 to 2.5 μm. Assuming DLA and a fractal dimension (D_f) = 1.67, eq 1 and 2 yield an R_H of 1.2−1.5 μm at 3.75 min. This estimated R_H is in good agreement with the DLS result (Figure S4b) which reports the upper end of the R_H distribution to be approximately 1 μm. After 9 min, some chain-like aggregates begin to form, while the individual micrometer-sized aggregates are still present (Figure 2c). This is also consistent with the DLS result at 10.5 min (Figure S4b) showing an increase of hydrodynamic radius to ∼1 μm and aggregates of up to 4.0 μm. After 30 min, the gelation of chain-like aggregates was observed (Figure 2d) where the length of the chains in the network varies from around 15−50 μm. Aggregation of particles in dispersions with a higher initial concentration (430 mg/L, $\Phi = 6.9 \times 10^{-5}$) was more rapid than at 60 mg/L, but the overall chain-like morphology of the aggregates appears to be the same (Supporting Information Figure S5).

Effect of Aggregation and Structure Evolution on the Sedimentation of NZVI Dispersions. The effect of aggregation and gelation on the sedimentation of NZVI dispersions was investigated by monitoring the sedimentation rates of nanoparticle dispersions with different initial particle con-

centrations (Figure 3a). The sedimentation curves of RNIP have three distinct regions (aggregation I, sedimentation I, and sedimentation II) for the concentrated dispersions (190−1130 mg/L), while that of the most dilute dispersion (4 mg/L) consists of only one region. This characteristic is also true for magnetite and hematite dispersions (Supporting Information Figure S6). In the aggregation I region, the sedimentation rate is low. During this time, the particles aggregate to form the chain-like aggregates as observed with the optical microscope, but largely remain suspended. Eventually, at a time t_{crit}, the chain-like aggregates gel to reach a critical size where sedimentation of the chain-like aggregates becomes rapid (sedimentation I). The critical time shortens as the initial particle concentration increases due to the more rapid aggregation at the higher concentration. At the end of the sedimentation I region, the sedimentation rate becomes low again, and this probably corresponds to the sedimentation of aggregates which did not form critical size chain-like clusters. For initial particle concentrations of less than about 7.5 mg/L, the aggregates never reach a critical size and are only slowly sedimented from solution (Supporting Information Figure S7).

The magnitude of the effect of the dispersion concentration and the magnetic attraction between the particles can be evaluated by comparing t_{crit} for RNIP, magnetite, and hematite at different initial concentrations. As shown in Figure 3(b), using least-squares fitting, t_{crit} and particle concentration are related by a power law with the exponents of -0.83, -1.05, and -1.29 for RNIP, magnetite, and hematite, respectively. Even at low concentrations of RNIP (80 mg/L), aggregation of nanoparticles into clusters that are large enough to be affected by gravity occurs in less than 30 min. At high particle concentrations that would be used in site remediation ($\sim$g/L range), particle aggregation and sedimentation occurs very rapidly ($t \sim$3 min).

The effect of magnetic attractive forces on aggregation and sedimentation can be determined by comparing t_{crit} for RNIP ($M_s = 570$ kA/m), magnetite ($M_s = 330$ kA/m), and hematite ($M_s = 14$ kA/m) at similar concentrations (Figure 3b). The t_{crit} observed for hematite dispersions (nonmagnetic) is significantly higher than for magnetite or RNIP dispersions which are magnetic. The order of increasing t_{crit} hematite > magnetite > RNIP follows their relative magnetization, indicating that the magnetic attractive forces between particles affects their aggregation and gelation and resulting tendency to sediment.

Unlike dilute dispersions, the hydrodynamic radius of the aggregates formed in concentrated suspensions cannot be measured directly with DLS due to multiple scattering. The size of the fractal aggregates formed in the concentrated slurry can, however, be estimated from the sedimentation curves. Obeying the two local conservation equations for mass and linear momentum, an equation to describe the local concentration of sedimenting particles as a function of time can be expressed as (27)

$$C_{(t)} = C_0 e^{-t/\tau} \quad (3)$$

where $C_{(t)}$ is the concentration of the sedimenting phase at time t, C_0 is the initial particle concentration at the beginning of the sedimentation region, and for a fractal aggregate with hydrodynamic radius R_H, the characteristic time, τ, is given by

$$\tau = \frac{9\eta(\beta - p_f)}{2g^2(\rho_s - \rho_l)^2 R_H^2} \quad (4)$$

where η is the solvent viscosity, β is a function of the permeability of the fractal aggregate (26−29), p_f is the fluid pressure, ρ_s and ρ_l are density of solid component and liquid, and g is the acceleration due to gravity.

Since each region of the sedimentation curve (Figure 3a) for concentrated RNIP dispersions (190−1130 mg/L) can be fitted by exponential decay (eq 3), we can calculate τ for each region and thus estimate the average R_H of fractal aggregates sedimenting in each region if β is known. Based on the R_H measured by DLS for the dilute dispersions (2−74 mg/L) of RNIP, and on the τ obtained from fitting sedimentation curves for RNIP at these dispersion concentrations (Supporting Information Table S1), there is a linear relationship between the measured average R_H and fitted β of the fractal aggregates formed (Figure 3c) given by eq 5 where R_H is in meters.

$$\beta = 5 \times 10^9 (R_H) - 1.5 \times 10^3 \quad (5)$$

Fluid flows more easily through a fractal aggregate with higher permeability and the aggregate experiences less hydrodynamic drag force so permeable fractal aggregates sediment faster than impermeable spheres (26, 29). Since the porosity of fractal aggregates increases radially from a dense core to sparse outer edges (26), the permeability (β) should increase

as R_H increases as in eq 5. By extrapolating this relationship to the more concentrated dispersions where R_H of the fractal aggregates cannot be directly measured using DLS, we can obtain a rough estimation of the average R_H from τ of each region as summarized in Figure 3d. The values of τ determined from fitting the sedimentation data in each region and for each concentration is provided in the Supporting Information (Table S2). To verify the accuracy of the predicted R_H values, the estimated R_H (Figure 3d, open boxes) in the Sedimentation II region for various initial RNIP concentrations (based on the measured τ) is compared with those measured by DLS after $\sim$2 h when the remaining RNIP concentration is low enough to avoid multiple scattering (Figure 3d, boxes with hash marks). The measured values ($R_H = 9.8-12.9\,\mu$m) agrees well with the estimates using this method ($R_H = 7.6-9.3\,\mu$m). The measured particle size distributions and the summary of average R_H used in this evaluation are provided in Supporting Information Figure S8 and Table S3.

Influence of Intrinsic Magnetic Attraction on Rapid Aggregation and Sedimentation of Aqueous NZVI Dispersions. The rapid aggregation of RNIP compared to the magnetite and hematite dispersions at similar initial particle concentrations can be explained using extended DLVO theory and statistically validated using multiple regression analysis.

Extended DLVO Theory. The time scale of colloidal dispersion stability is determined by the magnitude of the energy barrier between particles. According to classical DLVO theory, the major attractive energy is the van der Waals energy (V_{vdW}) while the major repulsive energy is electrostatic double layer interaction energy (V_{ES}) (6, 8, 13) The V_{vdW} attractive energy between spherical particles can be expressed as (13

$$V_{vdW} = \frac{-A}{6}\left[\frac{2a^2}{s(4a + s)} + \frac{2a^2}{(2a + s)^2} + \ln s\frac{(4a + s)}{(2a + s)^2}\right] \quad (6)$$

) where A is the Hamaker constant, which is 10^{-19} N·m for Fe, γ-Fe$_2$O$_3$ and Fe$_3$O$_4$ (11), a (m) is the radius of particles, and s (m) is distance between surface of two interacting particles. Electrostatic repulsion between two identical particles can be expressed as (13)

$$V_{ES} = 2\pi\epsilon_r\epsilon_o a\dot{\zeta}^2\ln[1 + e^{-\kappa s}] \quad (7)$$

where ϵ_r is the relative dielectric constant of the liquid, ϵ_0 is the permittivity of the vacuum, ζ, the zeta potential, is assumed to equal the surface potential of the charged particles, and κ is the inverse Debye length. Applying classical DLVO theory and assuming spherical particles, an energy barrier of $\sim$7.0 k_BT is predicted for RNIP (Figure 4) where k_B is the Boltzmann constant (1.38×10^{-23} m^2 kg s^{-2} K^{-1}). This applies to single particle−particle interactions and not necessarily to particle−aggregate interactions which are more complicated; however, the trends will be the same for each case. This energy barrier corresponds to a stability ratio of $\sim$90, i.e., aggregation of particles with this energy barrier is predicted to be 90 times slower than for particles aggregating under DLA without an energy barrier, suggesting that dispersions of these particles should be stable. This contrasts with the observed behavior. Slightly larger energy barriers are predicted for magnetite and for hematite (Figure 4, solid lines).

Iron nanoparticles that behave as a single domain magnetic particle have an intrinsic permanent magnetic dipole moment $\mu = (4\pi/3)r^3M_s$ even in the absence of an applied magnetic field (10, 11, 15, 16). r(m) is the radius of the particle and equal to a in eqs 6 and 7. When particle dipoles are oriented in a head-to-tail configuration, the maximum magnetic attraction energy (V_M) can be expressed as (13)
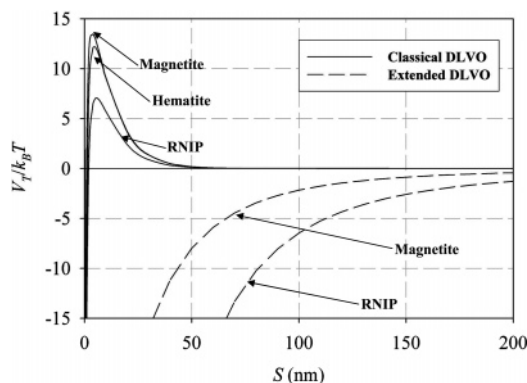
FIGURE 4. Potential energy of interaction for a pair of RNIP particles according to classical DLVO theory and extended DLVO theory when particle dipoles are oriented in head-to-tail configuration. The parameters used in this simulation are as follows: r = 20 nm for RNIP and hematite, r = 13.75 nm for magnetite, A = 10^{-19} N·m, ζ = −31.7, 38.2, and 39 mV for RNIP, magnetite, and hematite, respectively, M_S = 570, 330, and 14 kA/m for RNIP, magnetite, and hematite, respectively. The potential interaction energy of hematite modeled by classical and extended DLVO are not significantly different.

$$V_M = \frac{-8\pi\mu_0 M_s^2 r^3}{9\left(\frac{S}{r}+2\right)^3} \tag{8}$$

where μ_0 is the permeability of the vacuum. The potential energy interaction for RNIP that includes this magnetic attraction is also shown in Figure 4 (dashed lines). For magnetic nanoparticles such as RNIP and magnetite the magnetic attraction dominates the interaction energy, and there is no longer a predicted energy barrier to aggregation. This is in agreement with the rapid aggregation observed for these particles. This analysis assumes an ionic strength of 1 mM to correspond to that used in the experiments. At ionic strengths typical for groundwater, ~10 mM, aggregation would be even more rapid.

Multiple Regression Analysis. Aggregation and subsequent sedimentation of iron-based nanoparticle dispersions depend on of their radius, r (nm), their ζ potential (absolute value, mV), the initial volume fraction (Φ), which is proportional to the concentration of dispersion, the particle density, ρ_s (g/cm³), and the magnetization, M_s, (kA/m). Because t_{crit} is the time when the aggregates or structural networks reach a critical size with respect to gravitational sedimentation, it is influenced by how rapidly the nanoparticles transform to micrometer-size aggregates in the first regime, and how fast the micrometer-size aggregates assemble to fractal clusters or chain-like networks in the second aggregation regime. Thus, an empirical relation can be determined using t_{crit} (min) as a dependent variable together with the measurable parameters governing colloidal interaction and the kinetics of aggregation and sedimentation.

$$\text{Log } t_{crit} = K + B_\Phi \text{ Log } \Phi + B_r \text{ Log } r + B_{M_s} \text{ Log } M_s + B_\zeta \text{ Log } \zeta + B_{\rho s} \text{ Log } \rho_s \tag{9}$$

B_Φ, B_r, B_{M_s}, B_ζ, and $B_{\rho s}$ are unstandardized regression coefficients for Φ, r, M_s, ζ, and ρ_s, respectively. From the analysis, K, B_Φ, B_r, and B_{M_s} are 1.677, −0.904, −2.555, and −0.445, respectively. The standardized regression coefficients (β'), which indicate the normalized influence of each of the independent parameters on the dependent parameter such that they can be directly compared, are −0.607, −0.367, and −0.610 for Φ, r, and M_s, respectively. The two-tailed p-values (p) for Φ, r, and Ms is 0.000. Details of the input and the

results for the nonlinear multiple regression as well as the validation are available in the Supporting Information (Table S4−S6 and Figure S9). ζ (mV) and ρ_s (g/cm³) are excluded from the analysis by the SPSS because the slight variation of ζ and ρ_s between the nanoparticles studied here were not sufficient to significantly affect t_{crit}. Thus, the physical parameters which govern the difference among t_{crit} of these iron-based nanoparticles are Φ, r, and M_s. The magnitude of β' for each independent variable indicates how significant that independent variable is to the dependent variable. The influence of M_s (β' = −0.610) over t_{crit} is as significant as that of Φ (β' = −0.670), indicating that the magnetic attractive forces between NZVI particles affect its ability to form stable dispersions as significantly as increasing the concentration. This study used relatively oxidized RNIP (Fe^0 = 14%), so fresh RNIP with a higher Fe^0 content and larger saturation magnetization would be expected to aggregate even more rapidly than observed in this study. Thus, while a high Fe^0 content is desirable for remediation to deliver more electron equivalents for reducing contaminants, it will also increase the rate of aggregation of the particles.

The rapid aggregation of NZVI (consisting of ~20 nm primary particles) into micrometer-sized fractal aggregates has several implications. For example, in response to concerns about the environmental fate of nanomaterials, deep-bed filtration models have been used to estimate transport distances and sticking coefficients of nanomaterials in water-saturated porous media (5, 7, 30). These models assume that the particle size is fixed as the primary particle radius. However, given the rapid aggregation of NZVI into micrometer-sized fractal aggregates, it may be more appropriate to specify the aggregate size since the choice of particle size greatly affects the estimated effective mobility of the particles. Further, this rapid aggregation necessitates the use of adsorbed polymers to modify the NZVI surfaces (7, 31), or supported NZVI (5), to inhibit aggregation and improve mobility. Further advances in synthesis of reactive NZVI should consider ways to decrease their magnetization (e.g., the use of dopants or ways to synthesize multiple domain particles) as a means to improve the dispersion stability. However, methods to minimize attachment of NZVI to aquifer minerals would still be needed (7).

Supporting Information Available

UV−vis calibration curves, magnetization loops, and DLS raw data for RNIP, magnetite, and hematite; optical micrgographs of RNIP aggregation at 426 mg/L, sedimentation curves, raw data for fitting R_H vs β; estimated R_H, measured R_H for model verification, and regression analysis. This material is available free of charge via the Internet at http://pubs.acs.org.

Literature Cited

(1) Liu, Y.; Majetich, S. A.; Tilton, R. D.; Sholl, D. S.; Lowry, G. V. TCE dechlorination rates, pathways, and efficiency of nanoscale iron particles with different properties. *Environ. Sci. Technol.* **2005**, *39*, 1338−1345.

(2) Zhang, W.-X. Nanoscale iron particles for environmental remediation: an overview. *J. Nanopart. Res.* **2003**, *5*, 323 − 332.

(3) Ponder, S. M.; Darab, J. G.; Mallouk, T. E. Remediation of Cr(VI) and Pb(II) aqueous solutions using supported, nanoscale zero-valent iron. *Environ. Sci. Technol.* **2000**, *34*, 2564−2569.

(4) Henn, K. W.; Waddill, D. W. Utilization of nanoscale zero-valent iron for source remediation - A case study. *Rem. J.* **2006**, *16*, 57−77.

(5) Schrick, B.; Hydutsky, B. W.; Blough, J. L.; Mallouk, T. E. Delivery vehicles for zerovalent metal nanoparticles in soil and groundwater. *Chem. Mater.* **2004**, *16*, 2187−2193.

(6) Elimelech, M.; Gregory, J.; Jia, X.; Williams, R. *Particle Deposition and Aggregation: Measurement, Modeling, and Simulation*; Butterworth-Heinemann: Boston, 1995.

(7) Saleh, N.; Sirk, K.; Liu, Y.; Phenrat, T.; Dufour, B.; Matyjaszewski, K.; Tilton, R. D.; Lowry, G. V. Surface modifications enhance nanoiron transport and NAPL targeting in saturated porous media. *Environ. Eng. Sci.* in press.

(8) Strenge, K. Structure formation in disperse systems. In *Coagulation and Flocculation: Theory and Applications.*; Dobiáš, B., Ed.; Marcel Dekker: New York, 1993.

(9) Nurmi, J. T.; Tratnyek, P. G.; Sarathy, V.; Baer, D. R.; Amonette, J. E.; Pecher, K.; Wang, C.; Linehan, J. C.; Matson, D. W.; Penn, R. L.; Driessen, M. D. Characterization and properties of metallic iron nanoparticles: Spectroscopy, electrochemistry, and kinetics. *Environ. Sci. Technol.* **2005**, *39*, 1221−1230.

(10) McCurrie, R., A. *Ferromagnetic Materials: Structure and Properties*; Academic Press: London, 1994.

(11) Rosensweig, R. E. *Ferrohydrodynamics*; Cambridge University Press: New York, 1985.

(12) Beke, D. L. Intrinsic and domain magnetism in nanocrystalline materials. *Cryst. Res. Technol.* **1998**, *33*, 1039−1059.

(13) de Vicente, J.; Delgado, A. V.; Plaza, R. C.; Durán, J. D. G.; González-Caballero, F. Stability of cobalt ferrite colloidal particles: Effect of pH and applied magnetic fields. *Langmuir* **2000**, *16*, 7954−7961.

(14) Promislow, J., H., E.; Gast, A., P.; Fermigier, M. Aggregation kinetics of paramagnetic colloidal particles. *J. Chem. Phys.* **1995**, *102*, 5492−5498.

(15) de Gennes, P.-G.; Pincus, P. A. Pair correlations in a ferromagnetic colloid. *Phys. Kondens. Mater.* **1970**, *11*, 189−198.

(16) Butter, K.; Bomans, P. H.; Frederik, P. M.; Vroege, G. J.; Philipse, A. P. Direct observation of dipolar chains in iron ferrofluids by cryogenic electron microscopy. *Nat. Mater.* **2003**, *2*, 88−91.

(17) Chantrell, R. W.; Bradbury, A.; Popplewell, J.; Charles, S. W. Agglomerate formation in a magnetic fluid. *J. Appl. Phys.* **1982**, *53*, 2742−2744.

(18) Sandkühler, P.; Sefcik, J.; Morbidelli, M. Kinetics of gel formation in dilute dispersions with strong attractive particle interactions. *Adv. Colloid Interface Sci.* **2004**, *108−109*, 133−143.

(19) Allain, C.; Cloitre, M. The effects of gravity on the aggregation and the gelation of colloids. *Adv. Colloid Interface Sci.* **1993**, *46*, 129−138.

(20) Li, R.; McCoy, B. J.; Diemer, R. B. Cluster aggregation and fragmentation kinetics model for gelation. *J. Colloid Interface Sci.* **2005**, *291*, 375−387.

(21) Kim, M.; Corapcioglu, M. Y. Gel barrier formation in unsaturated porous media. *J. Contam. Hydrol.* **2002**, *56*, 75−98.

(22) Clarke, J.; Braginski, A. I. *The SQUID Handbook: Fundamentals and Technology of SQUIDs and SQUID Systems*; Wiley-VCH: New York, 2004.

(23) Farrell, J.; Kason, M.; Melitas, N.; Li, T. Investigation of the long-term performance of zero-valent iron for reductive dechlorination of trichloroethylene. *Environ. Sci. Technol.* **2000**, *34*, 514−521.

(24) Dunlop, D. J. Hysteresis properties of magnetite and their dependence on particle size: A test of pseudo-single domain remanence models. *J. Geophys. Res.* **1986**, *91B*, 9569−9584.

(25) Butler, R. F.; Banerjee, S. K. Theoretical single-domain grain size range in magnetite and titanomagnetite. *J. Geophys. Res.* **1975**, *80*, 4049−4058.

(26) Kim, A. S.; Yuan, R. Hydrodynamics of an ideal aggregate with quadratically increasing permeability. *J. Colloid Interface Sci.* **2005**, *285*, 627−633.

(27) Nicolosi, V.; Vrbanic, D.; Mrzel, A.; McCauley, J.; O'Flaherty, S.; McGuinness, C.; Compagnini, G.; Mihailovic, D.; Blau, W. J.; Coleman, J. N. Solubility of $Mo_6S_{4.5}I_{4.5}$ Nanowires in Common Solvents: A Sedimentation Study. *J. Phys. Chem. B.* **2005**, *109*, 7124−7133.

(28) Bürger, R. Phenomenological foundation and mathematical theory of sedimentation-consolidation processes. *Chem. Eng. J.* **2000**, *80*, 177−188.

(29) Li, X.-Y.; Logan, B. E. Permeability of fractal aggregates. *Water Res.* **2001**, *35*, 3373−3380.

(30) Lecoanet, H. F.; Wiesner, M. R. Velocity Effects on Fullerene and Oxide Nanoparticle Deposition in Porous Media. *Environ. Sci. Technol.* **2004**, *38*, 4377−4382.

(31) Saleh, N.; Phenrat, T.; Sirk, K.; Dufour, B.; Matyjaszewski, K.; Tilton, R. D.; Lowry, G. V. Adsorbed triblock copolymers deliver reactive iron nanoparticles to the oil/water interface. *Nano Lett.* **2005**, *12*, 2489−2494.